

Chapter 5. Modeling and validation of RF nanoelectronic devices

5.1 Introduction

The development and engineering of nanoelectronic devices has been characterized by several significant technological trends. In addition to the ongoing scaling of feature sizes down to nanoscale dimensions, the need for superior performance has driven the integration of novel materials as well as the incorporation of additional device functionalities. In turn, these trends require advanced manufacturing technologies. At the same time, the clock frequencies of nanoelectronic devices have increased into the microwave and millimeter-wave range. Importantly, these trends affect not only the engineering of active devices, but also the design of interconnects between devices.

Device and interconnect scaling leads to challenges in device engineering. For example, low-dimensional systems such as nanowires manifest new and altered material properties with respect to the bulk phase. Quantum effects that may not be evident in bulk material can have a significant influence as the diameter of a wire becomes less than several tens of nanometers. In addition, the conductivity can change substantially at these scales. In metallic nanowires, this is due to a decrease of the mean free path of electrons, while in carbon nanotubes (CNTs) such changes reflect the ballistic nature of electron transport. For example, the input impedance of a copper antenna of length 0.47λ changes from about $70 -j8$ Ohms to about $20,000 -j20,000$ Ohms as the diameter changes from $7.5 \mu\text{m}$ to 4nm [1]. Clearly, this presents significant challenges to scaling of copper-based radio frequency (RF) interconnects. Additional challenges arise due to contact impedance. While contact impedance often has a negligible effect at macroscopic scales, it can impact or even govern the RF response of nanoelectronic devices. This is due in large part to the fact that the size of a nanoelectronic device and the size of a contact are often comparable. In addition, in special cases such as molecular devices, atomically small changes in the positioning of the contacts can critically influence the performance of the device. Finally, as we have noted in previous chapters, the impedance of nanoscale devices is significantly different from the 50Ω impedance of the measurement equipment, thereby creating an inherently large impedance mismatch.

In the preceding chapters, we have demonstrated how metrology plays a crucial role in meeting these engineering challenges and enabling the understanding of material properties, circuits, interconnects, devices and antennas at nanoscale dimensions [2]. In addition to providing insight into new nanoscale phenomena, reliable high-frequency measurements can provide a foundation for comparing results and building consensus between different research endeavors. The inherent challenges of nanoscale measurements are further augmented by the need to make measurements at practical operating frequencies in the microwave and millimeter-wave range. In this chapter, we present a crucial piece of RF metrology for nanoelectronics: computational modeling and simulations.

Reliable models are required for the design of reliable and accurate test platforms, measurement calibration and verification, as well as the extraction of quantitative circuit and material parameters from measurements. In short, without modeling and simulation, we cannot fully address the critical measurement challenges of RF nanoelectronics. We present approaches suitable for characterization of

nanoscale devices, including nanowire-based interconnects and active nanotransistor devices. The focus is on the development of measurement models and methods for determination of constitutive material and device parameters. In the previous chapter, we investigated the extension of established measurement techniques to on-wafer nanoelectronic devices. Here, we use modeling to validate that approach, complementing the measurement techniques and establishing a complete measurement framework. Both full-wave, finite-element models and circuit models are used to determine the properties of nanoelectronic systems. These models are then compared with calibrated measurements in order to validate the measurement and calibration procedures. Passive, two-port test structures based on Au microbridges and Pt nanowires are used as illustrative examples. As will become evident below, the separation of the intrinsic properties of nanowires from the properties of electrical contacts presents a significant challenge. To address this problem, we present two approaches based on transmission line and circuit models. Though the modeling of any particular problem will present unique aspects, the examples presented here should provide a foundation that can be extended to address individual, specialized cases. For example, these methods can be extended to RF applications based on semiconducting nanowire devices, two dimensional materials, or other emerging materials.

5.2 Modeling and validation of measurement methods

5.2.1 Electromagnetic properties of nanoscale conductors

We begin by addressing the basic question of transport and impedance in one-dimensional systems and related devices. One-dimensional systems such as nanowires are a fundamental building block for micro- and nanoscale systems with a broad range of applications including sensors, field effect transistors, packaging, and flexible substrates [3]-[9]. The electrical properties of such systems depend on elemental composition, size, and morphology. If the dimensions of a nanowire are on the order of the quantum mechanical wavelength of an electron, the DC resistance is on the order of $h/2e^2 \approx 12.5 \text{ k}\Omega$, assuming a single conduction channel (h is Planck's constant and e is the charge of an electron). If the number of conduction channels is increased, as when one accounts for spin, then this resistance is divided by the number of channels. This extreme resistance is far from the impedance of commercial, $50 \text{ }\Omega$ test equipment and such extreme impedance mismatch influences device design, modeling and measurement. In spite of the large resistance, the operating frequency of nano-electronic devices can extend to the terahertz regime due to their low capacitance, which is on the order of tens of attoFarads to few femtoFarads. This opens the possibility of extremely high-frequency transistor applications.

We will follow the approach of Reference [10] that was developed for CNTs, but is applicable to nanowires and other low-dimensional systems. As a starting point, a simple transmission line models is used. In some cases, such as single-walled CNTs and THz systems, the model is modified to include a kinetic inductance in series with the per-unit-length resistance and per-unit-length inductance. Furthermore, a quantum capacitance may be added in series with the per-unit-length capacitance. Values of the per-unit-length inductance and per-unit-length capacitance depend on the geometry of the system and can be evaluated through analytical calculations, finite-element modeling, or measurement. The kinetic inductance per-unit-length for one-dimensional systems with a single conduction channel can be expressed as

$$L_K = \frac{h}{2e^2 v_F} \quad , \quad (5.1)$$

where v_F is the Fermi velocity. As with the quantum resistance, if the number of channels is greater than one, then L_K is divided by the number of channels. As an example, L_K is about 16nH/ μm in single-layer graphene. The quantum capacitance arises from the fact that for a low-dimensional quantum system one can add an electron to the system only if its energy is above the Fermi level. In general, the relation is complicated, but the quantum capacitance per unit length is proportional to density of states (DOS):

$$C_Q \approx e^2 \text{DOS} \quad . \quad (5.2)$$

For a single-walled CNT the expression for C_Q is $2e^2/(hv_F)$, which is about 100 aF/ μm . The total capacitance per unit length is the series combination of the per-unit-length electrostatic capacitance, which depends on the geometry of the system, and the quantum capacitance. Note that if one considers only the kinetic inductance and quantum capacitance, the characteristic impedance of an individual, single-walled CNT is on the order of 12.5 k Ω .

In general, the effects of kinetic inductance and quantum capacitance must be handled on a case-by-case basis. When determining whether these terms must be included in the transmission line model, one must consider the distributed resistance of the microwave structure into which nanoscale building block is embedded and the relative sizes of the mean free path of the carriers and the device dimensions. Further details about the role of quantum capacitance and inductance in transmission line models are discussed in References [10] and [11]. Lastly, in many cases the contact impedance in low-dimensional components also has to be taken into account [2], [11].

5.2.2 An overview of validation

The validation of high frequency measurement and calibration methods is a critical component of quantitative metrology for RF nanoelectronics, particularly if the applications cover a broad range of operation frequencies. One cannot simply assume that established approaches for measurement and calibration of connectorized and on-wafer RF devices are valid for nanoelectronics. The validation step is all the more crucial because of the extreme impedance mismatch of nanoelectronics with respect to host structures and commercial test equipment. Matching networks can ameliorate this problem in a narrow frequency range, as discussed in Chapter 3, but for broadband measurements the device will always represent an extreme impedance load. Below, we discuss the validation of measurement and calibration methods, building upon the introduction of several such measurement approaches in the previous chapters.

Modeling and simulation accomplish two main objectives related to measurement of extreme impedance loads, in general, and RF nanoelectronics, in particular. The first is the validation of the calibration methodology and the second is the extraction of circuit and material parameters from the measurements. For example, for metallic nanowires, one may need to extract the wire conductivity and the contact resistance. Validation requires the design of appropriate models and the comparison of the models' predictions to calibrated measurements. These models require reliable inputs that accurately represent devices and their constituent structures, including geometry and material parameters. In order to focus the measurement and modeling problems on the nanoscale components, in most cases the fixtures that are the part of the nanoscale test structures are de-embedded and the reference planes are moved as

close as possible to the nanoscale elements of interest. If significant differences between the model predictions and the calibrated measurements are observed, then either the modeling or measurement approach must be discarded as unsuitable for characterization of nanoscale devices. For example, an established calibration procedure may be unsuitable if the underlying assumptions of the calibration process are invalid. One critical question is whether the propagating electromagnetic field corresponds to a single mode or if higher order modes are also present. Single-mode propagation is a fundamental assumption of multilayer thru-reflect-line (TRL) and other established calibration procedures. In addition, the field distribution of the fundamental mode must be investigated, as in many nanoscale devices this distribution will violate the assumption of pure TEM-mode propagation.

Once the measurement and calibration methods are validated, one can proceed to the extraction of device parameters. To extract such parameters, calibrated measurements of the device scattering parameters are compared with full wave and circuit model simulations. For example, for conducting and semiconducting nanowires a range of the conductivities can be obtained by fitting the contact resistance and wire resistance to measured data, minimizing the deviation between the models and measurements. Note that if the model has too many unknown parameters, this approach may not have a unique solution and therefore additional measurements or methods have to be used, as discussed below. Several modeling approaches are applicable here: full-wave finite element models, equivalent lumped element circuit models, and transmission line models.

5.2.3 Validation with finite element models

As a first example, we focus on the validation of multilayer TRL calibration by use of full-wave, finite element modeling (FEM), but the techniques can be generalized to other on-wafer calibration techniques. We assume that coplanar waveguides (CPWs) of different lengths along with appropriate coplanar short and open circuits are used as calibration standards. The on-wafer segment of the fixtures of the nanoelectronic devices under test (DUTs) are required to have the same CPW geometry as the calibration structures. All calibration structures are assumed to be fabricated on the same substrate as the fixtured, nanoelectronic DUTs.

Fig. 5.1(a) shows an example of a nanoelectronic DUT: a gold (Au) microbridge embedded in a two-port, CPW host structure. The center conductor of the CPW host is tapered such that it is just a two-micrometer-wide, four-micrometer-long strip at its narrowest point. The structure is fabricated on a quartz substrate by use of lithographic patterning, thin film sputtering, and liftoff. Fig. 5.1(b) shows a second test structure: a bridge-free, empty device that serves as a reference device for measurements and modeling as described below. For the purpose of validation, it is instructive to start with the modeling of simple structure like the Au microbridge. The microbridge represents a DUT with extreme impedance, albeit an extremely low impedance with respect to 50 Ω . Further, the Au bridge is continuous with the host structure, removing any complicating contact effects. The empty structure is identical except for the removal of the Au bridge and serves as a complementary DUT with an extremely high impedance. Using these two simple configurations, one can investigate both impedance extremes and test different numerical methods. Like many RF nanoelectronic devices, the reflection coefficient is high for both of these device configurations, thus providing further confidence that the validation methods may be applied to a broad range of nanoscale systems.

Figure 5.1. **Au microbridge device and an empty reference device.** (a) Optical microscope image of a lithographically-patterned, two-port Au device in which a 2 μm -wide bridge connects tapered segments of a CPW center conductor. The inset illustrates the device geometry. (b) Optical microscope image of a Au reference device without the Au bridge.

It is possible to model the broadband characteristics of this device by use of a number of commercial software packages, including RF finite-element-based software such as HFSS [12], CST Microwave Studio, AWR Microwave Office, COMSOL, and JCMSuite [13], as well as circuit-based software such as Spice, ANSYS Designer [14], and AWR Microwave Office [15].¹ Among these packages, the full-wave numerical methods such as finite element electromagnetic solvers are advantageous due to their three-dimensional modeling capability. FEM methods are based on the solution of three-dimensional wave equations and enable accurate analysis both of open and closed boundary value problems. They offer the possibility to treat inhomogeneous materials and a wide variety of shapes over a broad frequency range. The calculated field expansion is done using polynomials of different orders and users have access and control at different stages of the solution process. For on-wafer problems such as those treated here, it is useful to reduce the computational overhead associated with meshing by replacing the on-wafer probes with ideal wave ports.

The detailed steps of FEM calculations require familiarity with the modeling software, device layout and calculation steps. Such details are beyond the scope of this book, but it is instructive to present results from numerical modeling of example nanoelectronic devices. Following References [16] and [17] the scattering parameters of the Au microbridge and empty DUTs were modeled by a commercial FEM package over a frequency range of 50 MHz to 50 GHz. The results were compared to broadband, on-wafer, multiline TRL calibration results, as shown in Fig. 5.2. The results of the comparison show excellent agreement between the model and the calibrated measurement can be achieved, confirming that the FEM approach is suitable for modeling of nanoelectronic devices with dimensions much smaller than the wavelength of the electromagnetic field. The agreement further suggests that there is no significant generation of higher order modes in these devices. Calculation of the electric field distribution in the vicinity of the microbridge and additional analysis shows that higher order modes transmit less than 10% of the incident power [18].

Figure 5.2. **Comparison of finite-element model and measurements for a gold microbridge device and an empty reference device.** Measured and simulated scattering parameters for (a) an “empty” device and (b) a gold microbridge device (labeled “Au short”). In the empty device, a dielectric (SiO_2) layer has been deposited in the CPW gap. Simulations (black squares) were carried out with commercial full-wave, finite-element modeling software. Measurements (open circles) were calibrated with the on-wafer, multiline TRL method. © 2010 IEEE. Reprinted, with permission from K. Kim, T. M. Wallis, P. Rice, C.-J. Chiang, A. Imtiaz, P. Kabos, and D. S. Filipovic, *IEEE Microw. Compon. Lett.* **20** (2010) pp. 178 – 180.

¹ The use of trade names is intended to provide clarity and does not constitute endorsement by NIST.

5.2.4 Validation with circuit models

Full-wave FEM solvers require significant computational resources due to large memory requirements and long computation times. Therefore, circuit models, which require less memory and have significantly shorter computation times, have their place in the toolbox of methods for high frequency device evaluation. However, it must be noted that circuit models often require input in the form of experimentally-determined or FEM-simulated parameters. Once again, the Au microbridge and the empty devices shown in Fig. 5.1 serve as the example test structure. Circuit models of the empty and nanowire devices are shown in Fig. 5.3. It is useful to introduce the parasitic gap capacitance in parallel with the contacted nanowire, as shown in the lower panel of Fig. 5.3, to represent the coupling between the two tapered waveguide segments of the host structure.

Figure 5.3. Circuit models for an empty reference device and a gold microbridge device. Circuit models for the empty device and the microbridge device are shown in the top and bottom panels, respectively. The test platform, including the fixtures and host structure are represented by an ideal port connected to a segment of transmission line, followed by a tapered transmission line on either side of the device. The empty device is represented by a capacitive coupling while the microbridge is represented by the same capacitive coupling in parallel with a transmission line and resistive contacts. In the case of the continuous microbridge, the resistance of the contacts is negligible. © 2011 IEEE. Adapted, with permission from K. Kim, P. Rice, T. M. Wallis, D. Gu, S. Lim, A. Imtiaz, P. Kabos, and D. S. Filipovic, *IEEE Trans. Microw. Theory Techn.* **59** (2011) pp. 2647-2654.

The value of the parasitic gap capacitance C_{gap} may be obtained from the comparison of the circuit model results with either the FEM simulation or the experiment. From FEM modeling, C_{gap} is 0.6 fF for the Au microbridge device, in good agreement with the value obtained by fitting calibrated measurements. In contrast, the value of C_{gap} from calculation of the electrostatic capacitance for the given device dimensions by use of standard circuit model libraries results in an estimated value of 5.3 aF, leading to poor agreement with the measurements. The reason for this discrepancy is that the circuit model fails to account for stray fields and the resulting parasitic coupling in devices with multiple, closely-spaced signal lines. This underscores the fact that for RF nanoscale devices, the impedance of the environment surrounding the nanoscale element plays an important role. For the circuit model approach, it is necessary to take care in estimating the circuit parameter values of nanoscale elements and their surrounding structural environments. Standard circuit libraries that are reliable for modeling more traditional microelectronics may be insufficient for modeling some nanoelectronic devices. When a reliable, experimentally-established estimate of the parasitic capacitance C_{gap} is used, the circuit models are found to be in good agreement with experimental results for the empty device, but the agreement is poorer for the Au microbridge. Furthermore, there are significant differences between the circuit model results for different software packages [18]. In summary, circuit models may serve as a useful, complementary tool in the validation process for RF nanoelectronic devices, but such models have significant limitations.

5.3 Extracting circuit parameters from measurements

5.3.1 Nanowire device parameters

With the validation of measurement methods demonstrated, one can proceed with the de-embedding of circuit and material parameters from broadband measurements of nanoscale devices. Without loss of generality, we will demonstrate extraction of circuit parameters for example devices that incorporate single nanowires and nanowire-like structures such as carbon nanotubes. The properties of several types of nanowire devices are summarized in Table 5.1. Note the wide variation in resistivity as well as contact resistance. For example, a Pt nanowire deposited on Au has a contact resistance of about 138 Ω , while a similar nanowire attached to Pt electrodes has a significantly higher contact resistance of 700 k Ω to 800 k Ω [24].

Table 5.1 **Resistivity and contact resistance for selected metallic nanowire devices.** Adapted from [18], with permission.

[Citation] (Year)	[19] (2000)	[20] (2003)	[21] (2003)	[22] (2004)	[23] (2007)	[24] (2008)
NW Material	Au	Cu	Pt	Pt	Pt	Pt
NW Diameter (nm)	70	60	60	70 \pm 5	60 – 360	80 – 150
Resistivity ($\mu\Omega$ cm)	4.5 (bulk: 2.5)	17.1 (bulk: 1.72)	61.5 (5.9 μm) 482 (13 μm) 545 (20 μm) (bulk: 10.8)	33 \pm 5	860 – 3078	Not Reported
Contact Resistance	Not Reported	Not Reported	Not Reported	138 Ω	Up to 100 Ω	700 k Ω – 800 k Ω

For nanowire structures these two quantities - the resistivity (or conductivity) of the nanowire and the contact resistance to the wire - are usually the parameters of greatest interest. The conductivity of the wire primarily reflects the specific material properties of the nanowire, though a full understanding of the device performance may require consideration of the kinetic inductance and quantum capacitance in selected cases, as described above and in References [2], [10], and [11]. Broadly speaking, contact resistance is a critical parameter for most nanoscale devices operating at RF and may vary strongly from device to device. One central problem of extracting these parameters is that the contact resistance is measured simultaneously with the intrinsic resistance of the device [16], [17], [20]. Additional measurements or alternative approaches are required to uniquely determine the wire conductivity and the contact resistance.

The example device we will discuss here incorporates an oxide-supported Pt nanowire deposited on Au electrodes, as shown in Fig. 5.4. It is nearly identical to the Au microbridge shown in the Fig. 5.1, but with the nanowire now serving as a bridge across a gap in the CPW center conductor. Pt nanowires with diameters of 150 nm and 250 nm were used. This two-port device is a useful model system as it represents a high impedance. In addition, this is an example of a system where the properties of the nanoscale

element must be fully de-embedded from the on-wafer test fixtures in order to extract material and circuit parameters.

Figure 5.4. **Pt nanowire device.** Scanning electron microscope image of a lithographically-patterned, two-port device that incorporates an oxide-supported Pt nanowire that bridges a gap in the CPW center conductor. The inset illustrates the device geometry.

5.3.2 Full-wave, finite element approach

As a first example of parameter extraction, we discuss estimation of the conductivity and contact resistance of the two-port Pt nanowire device by use of a full-wave, three-dimensional solver [9], [25]. The device dimensions, as determined from scanning electron microscope images, and the wire conductivity are inputs for the simulation. To simplify the analysis, excitation ports are used in place of the probe tips. Initially, the contact between the NW and the electrodes is assumed to be ideal, *i.e.* the contact resistance $R_c = 0 \Omega$. When the conductivity of the wire σ is set to the macroscopic, bulk Pt conductivity $\sigma = \sigma_{\text{bulk}} = 9.3 \times 10^6 \text{ S/m}$, there is an enormous discrepancy between the measurement and the calculations. For example, broadband, calibrated measurements from 100 MHz to 50 GHz reveal that $|S_{21}|$ for the Pt nanowire device is between -17 dBm and -20 dBm, while the finite element simulation with the bulk value of conductivity predicts that $|S_{21}|$ is about -2 dBm over the same frequency range. Even when the conductivity is reduced to $0.5 \sigma_{\text{bulk}}$, this discrepancy remains. To remove this discrepancy, σ must be further reduced and a nonzero contact resistance R_c can be introduced. To introduce the contact resistance into a full wave model, it is necessary to apply lumped element boundary conditions. Unfortunately, full-wave, finite-element simulations do not allow a unique separation of the contact resistance and conductivity. In other words, σ and R_c can vary over a large range and still fit the experimental data. This ambiguity is illustrated in Fig. 5.5(a). When the conductivity is σ_{bulk} , agreement with the experimental data is found with $R_c = 315 \Omega$. When the contact resistance is set to zero, agreement with the experimental data is found with $\sigma = 0.014 \sigma_{\text{bulk}}$. In this latter case, σ may at best be interpreted as an effective conductivity parameter that reflects the combined effects of wire conductivity, contact resistance, and other parasitic effects.

Figure 5.5. **Pt nanowire conductivity and contact resistance extracted by use of finite element models.** (a) Scattering parameter magnitudes $|S_{11}|$ and $|S_{21}|$ as a function of frequency. Two solution pairs of the conductivity σ and contact resistance R_c that simulate the measured data are shown. Reprinted from [18], with permission. (b) Sets of solution pairs for a 150 nm-diameter nanowire device and a 250 nm-diameter nanowire device. Literature A, B, and C correspond to References [21], [22], and [23], respectively. © 2011 IEEE. Reprinted, with permission from K. Kim, P. Rice, T. M. Wallis, D. Gu, S. Lim, A. Imtiaz, P. Kabos, and D. S. Filipovic, *IEEE Trans. Microw. Theory Techn.* **59** (2011) pp. 2647-2654.

This simple example serves as something of a cautionary tale. The contact resistance and the wire conductivity are in series and there is no possibility to separate them by use of a single measurement of a single device. Although the range of possible solutions is broad, the contact resistance and the wire conductivity are coupled. Specific solution pairs are shown in Fig. 5.5(b). This problem persists

independently of the calibration method used to de-embed the wire properties. As with full-wave, finite elements models, comparisons of circuit models to experimental data lead to a wide range of solution pairs for σ and R_c . Measurement strategies for separation of the contact resistance from the conductivity include measurement of wires of different length or measurements of a single device before and after treatment that systematically alters contact resistance or conductivity. These measurement strategies may be supplemented by alternative modeling approaches, such as transmission line and lumped element models, as described below.

5.3.3 Transmission line approach

Next, we outline a strategy for extraction of device parameters by use of a transmission line model. Importantly, the transmission line model requires an assumption that the characteristic impedance and propagation constant do not vary over the length of the wire. The first step in this strategy, as with several other approaches that we have described, is to translate the reference planes as close as possible the nanowire contacts. We denote the translated S-parameter matrix of the nanowire device as \mathbf{S}^{tot} and for an empty, nanowire-free device as \mathbf{S}^{empty} . Following the “empty device method” from Chapter 4, we convert these matrices to admittance matrices, \mathbf{Y}^{tot} and \mathbf{Y}^{empty} and then obtain the intrinsic admittance matrix for the nanowire and contacts, \mathbf{Y}^{NW} by subtraction of \mathbf{Y}^{empty} from \mathbf{Y}^{tot} (Alternatively, an approach based on the conversion of S parameter matrices to impedance matrices may be developed in a similar way). It is useful to transform \mathbf{Y}^{NW} into ABCD-matrix form: \mathbf{ABCD}^{NW} . We assume that the two contact resistances R_c are identical and in series with the nanowire. If the nanowire is represented by a transmission line of length l ,

$$\mathbf{ABCD}^{NW} = \begin{bmatrix} 1 & R_c \\ 0 & 1 \end{bmatrix} \cdot \begin{bmatrix} \cosh(\gamma l) & Z_0 \sinh(\gamma l) \\ \frac{1}{Z_0} \sinh(\gamma l) & \cosh(\gamma l) \end{bmatrix} \cdot \begin{bmatrix} 1 & R_c \\ 0 & 1 \end{bmatrix}, \quad (5.3)$$

where Z_0 and γ are the characteristic impedance and propagation constant of the nanowire transmission line, respectively. To separate the conductivity and contact resistance, we require two measurements on devices with nanowires of different lengths, l_1 and l_2 . Simple algebraic treatment leads to expressions for Z_0 and γ :

$$Z_0 = \sqrt{\frac{B^{NW}_i}{C^{NW}_i}} \quad (5.4)$$

and

$$\gamma_i = \frac{1}{l_i} \ln(A^{NW}_i \pm \sqrt{(A^{NW}_i)^2 - 1}) \quad (5.5)$$

$A^{NW}_i, B^{NW}_i, C^{NW}_i$ are elements of the measured ABCD matrix \mathbf{ABCD}^{NW} and the index $i=1,2$ enumerates the measurements made with the nanowires of different lengths. The propagation constant is assumed to be the same for both lengths ($\gamma = \gamma_1 = \gamma_2$). Expanding the \sinh and \cosh functions in equation (5.3) into Taylor series and retaining the terms to second order gives simplified expression

$$R_c = \Re \left\{ \frac{(l_1)^2 (A_{2-1}^{NW}) - (l_2)^2 (A_{1-1}^{NW})}{(l_1)^2 C_{2-1}^{NW} - (l_2)^2 C_{1-1}^{NW}} \right\} . \quad (5.6)$$

With R_c established, it is now possible to independently determine the conductivity of the nanowire by use of a full wave or circuit model.

It is necessary to consider the results from this approach very carefully: simple results can be deceiving. The result is sensitive to the terms in the denominator of equation (5.6) that are usually quite small. Highly accurate measurements are required and any noise introduced into the measurements makes it almost impossible to get reliable information about the device parameters. In addition, the transmission line model accounts only for a single propagating TEM mode, but full-wave modeling reveals that there may be multiple modes. In the case of multimode propagation, it is necessary either to use the multimode calibration procedure discussed in Chapter 2 or consider the single-mode results as a first approximation to the corrected measurements. Also note that the use of redundant measurements, introduced in Chapter 3, can further decrease the statistical uncertainty of the measurement. In summary, this approach, though analytically straightforward, may be practically unreliable for extracting the properties of the wires and contacts, even if multiple devices of different lengths are measured.

5.3.4 Lumped element approach

Because the length scale of nanoscale devices is usually much smaller than the wavelength of the propagating microwave signal, meshing in FEM simulations presents significant challenges related to memory requirements and computation times. On the other hand, the interaction of electromagnetic waves with a nanoscale device is described well in the electrostatic limit. Therefore, it is reasonable to assume that if one moves the calibrated reference planes as close as possible to the nanoscale device that a lumped element approach may work well. A hybrid approach that combines transmission lines and lumped elements may also be effective.

Figure 5.6. **Lumped element model of a two-port nanoelectronic device.** The contact resistances are represented by resistors R_c at either end of the device. The nanowire (or other nanoscale element) is represented by a T model with impedances Z_1 , Z_2 , and Z_3 .

In the lumped element approach, a simple two-port “T” or “ π ” model can be used to represent the nanowire. To the extent that nanowire devices can be assumed to be symmetric, such circuits can be significantly simplified. A schematic of a nanowire device represented by a two-port T model in series with contact resistances is shown in Fig. 5.6. Once again, we will require measurements of two (or more) devices of different lengths, indexed by $i = 1, 2$ (Z_{11} is the value of Z_1 for device of length l_1 , Z_{21} is the value of Z_1 for device of length l_2 , and so on). If each device is symmetric, $Z_{i1} = Z_{i2}$ and together with the shunt impedances Z_{i3} this fully characterizes each nanowire device. The ABCD matrices in terms of these impedances are

$$ABCD^{NW}_i = \begin{bmatrix} 1 + \frac{Z_{i1}}{Z_{i3}} & 2Z_{i1} + \frac{Z_{i1}^2}{Z_{i3}} \\ \frac{1}{Z_{i3}} & 1 + \frac{Z_{i1}}{Z_{i3}} \end{bmatrix} . \quad (5.7)$$

Following a similar procedure as in the transmission line approach and replacing the nanowire transmission line matrix in equation (5.3) with equation (5.7), the impedances associated with this model are related to the elements of the measured ABCD matrices through

$$Z_{i3} = \frac{1}{C^{NW_i}} \quad (5.8)$$

and

$$Z_{i1} = \frac{A^{NW_i} - R_c C^{NW_i} - 1}{C^{NW_i}} \quad (5.9)$$

Again using simple algebra, the contact resistance can be expressed as

$$R_c = \Re \left\{ \frac{l_2 C^{NW_2} (A^{NW_1} - 1) - l_1 C^{NW_1} (A^{NW_2} - 1)}{(l_2 - l_1) C^{NW_1} C^{NW_2}} \right\} \quad (5.10)$$

In a similar way, by taking the imaginary part instead of the real part of the expression in equation (5.10), the contact reactance is obtained. Since the wire's resistance is part of Z_{i1} , the wire conductivity can be obtained directly from the calculated impedances of the equivalent lumped-element T circuit in Fig. 5.6. Furthermore, validation of this approach can be done with a modified version of the circuit model in Fig. 5.3(b) in which the nanowire element is replaced by the T circuit. Validation with a full wave model is also possible, with little change to the procedure. The full-wave model validation shows that the simple circuit model approach works well and can be used for extraction of the nanowire and contact resistance with reasonable precision.

Following the lumped element approach, the extracted values of the conductivity and the contact resistance for the Au microbridges and Pt nanowire devices are shown in Fig. 5.7(a) and Fig. 5.7(b), respectively. Two device lengths were fabricated and measured for each system: 4.0 μm and 8.0 μm . To reduce statistical contributions to uncertainties, multiple devices were measured and multiple measurements were made of each device. The Pt nanowire conductivity was calculated assuming that the wires have a circular cross section. While the contact resistance of the Au microbridge is expected to be zero, the obtained result of 0.5 Ω is reasonable and well within estimated uncertainties.

Figure 5.7. Circuit parameters extracted by use of the lumped element approach. A lumped element approach was used to extract the contact resistance and conductivity for (a) Au microbridge device and (b) Pt nanowire device. © 2011 IEEE. Reprinted, with permission from K. Kim, P. Rice, T. M. Wallis, D. Gu, S. Lim, A. Imtiaz, P. Kabos, and D. S. Filipovic, *IEEE Trans. Microw. Theory Techn.* **59** (2011) pp. 2647-2654.

This lumped element approach assumes that there is little if any variation of the contact resistance from device to device and from contact to contact within a device. If we are only interested in isolating the properties of a nanowires or another nanoscale building block, it is desirable to design a device in such a way that the contact resistance would not come into play. One way to eliminate the contact resistance is

to contact the measured nanowire to the host structure by use of capacitive coupling. Such coupling can be realized through a dielectric layer between the nanowire and the signal line or by cutting slots in the signal line and positioning the nanowire between these slots. In principle, the use of capacitive contacts requires measurement of a single device rather than multiple devices of different lengths. The disadvantage of this approach is the underlying assumption that the contact reactance can be accurately determined from knowledge of the structural form and material properties of the contacts. In addition, all dielectric layers have to be well-characterized, uniform, and free from contaminants in order to estimate dielectric constants. Little if any DC current will flow through the device. Further, with increasing separation of the nanoscale element from the host, sensitivity to nanowire properties are decreasing rapidly.

The layouts of the Au microbridge and Pt nanowire devices can be modified to have capacitive contacts. The inset in Fig. 5.8 shows a scanning electron microscope image of a Au microbridge structure that has been modified with a focused ion beam such that there are slots that electrically separate the bridge element from the host CPW's center conductor. Calibrated measurements are compared with full wave simulations in Fig. 5.8. The high-level of agreement is encouraging, at least for this case of an extremely-low impedance device. In order to examine the case of extremely high impedance devices, Pt nanowire devices were fabricated with a dielectric layer between the wire and the conductive signal line of the host structure. For this case the critical parameter is the thickness of the dielectric separation layer and the length of the overlap of the nanowire with the signal line [17]. Measurements for the capacitively coupled Pt nanowire devices yielded values of Pt nanowire conductivity consistent with the results from the lumped element approach. Simulations further reveal that the frequency-dependent amplitudes of S_{11} and S_{21} are significantly more sensitive than the phases of S_{11} and S_{21} to changes in nanowire conductance.

Figure 5.8. Au microbridge device with capacitive contacts. Calibrated measurements and finite-elements simulations of the scattering parameters of a Au microbridge device. The inset shows a scanning electron microscope image of the device. The gold layer has been cut by use of a focused ion-beam in order to produce slots near the contact region, yielding contacts that are primarily capacitive. (Data courtesy of D. S. Filipovic, University of Colorado, Boulder)

5.3.5 Modeling and parameter extraction for carbon nanotube devices

Historically, nanoelectronic devices based on CNTs have been of widespread interest, due to their potential applications as high-frequency transistors, nanoantennas and interconnects. Single-walled carbon nanotubes present special problems that are not present in the more general case of nanowires. Previously we have discussed some of these problems, including high contact impedance and quantum mechanical effects. In order to extract reliable information from RF measurements of single-walled CNT devices, models must be altered by the modification of circuit and material parameters. The complex conductivity of metallic CNTs can be expressed as:

$$\sigma_{CNT}(\omega) = -j \frac{2e^2 v_F}{\pi^2 \hbar a (\omega - j\nu)} \text{ [S]} \quad , \quad (5.11)$$

where e is the charge of electron, ν is the relaxation frequency as defined in [26], ω is the angular frequency, \hbar is the reduced Planck's constant and v_F is the Fermi velocity. It is important to notice that the units of σ_{CNT} are S , not S/m . Equation (5.11) is derived under the assumption that the thickness of the CNT wall is zero and therefore only surface currents are present. Based on this definition, the surface impedance of the CNT can be expressed as

$$Z_{CNT} = \frac{1}{2\pi a \sigma_{CNT}} \left(\frac{\Omega}{m} \right) \quad (5.12)$$

As with nanowire devices, in order to de-embed the properties of CNT devices, it is necessary, in most cases to measure an empty, CNT-free device structure. The intrinsic, frequency-dependent impedance of a CNT vary widely from a few to hundreds of $k\Omega$ [27], which is consistent with theoretical predictions [28]. Note once again that the performance of CNT devices may critically depend on the quality of the electrical contacts.

So far, we have exclusively discussed nanoelectronics devices that incorporate a single CNT or other nanoscale building block. To reduce device impedance and loss, CNT bundles may be used in place of individual CNTs in interconnects as well as vertical vias in multilayered integrated circuits [29], [30], [31]. A CNT bundle may consist of as many as hundreds of CNTs. The resistance and inductance of the bundle are found to be inversely proportional to the number of CNTs [29], providing an avenue to produce device impedances that match 50Ω test equipment. A distribution of CNT types must be assumed. For example, in References [32] and [33], the distribution is assumed to be about one third metallic and two thirds semiconducting. For many applications, further improvement in electrical performance can be achieved by use of bundles made exclusively from metallic CNTs.

Figure 5.9. **Scattering parameters of a GaN nanowire device simulated with a genetic algorithm.** Simulated scattering parameters of the circuit models of a two-port GaN NW device compared to calibrated measurements: S_{11} (a,b) and S_{21} (c,d). A schematic of the circuit model obtained with the genetic algorithm is shown in the inset of (b). © 2011 IEEE. Adapted, with permission from T. M. Wallis, *2011 78th ARFTG Microwave Measurement Symposium* (2011) pp.1-5.

Measurement of CNT bundle devices may be performed by use of the same calibration and de-embedding techniques as discussed for individual nanowires and CNTs. For modeling and validation, it is assumed that each CNT has a four conduction channels and a corresponding quantum resistance of $6.45 k\Omega$. The kinetic inductance for each CNT is about $16 \text{ nH}/\mu\text{m}$ and quantum capacitance is about $100 \text{ aF}/\mu\text{m}$. Coupling between the wires is assumed to be negligible. Thus, the total resistance, inductance, and capacitance for a bundle may be determined from a simple model where all of the CNTs are in parallel. Additional, complementary approaches include multi-conductor transmission line models, equivalent single-conductor transmission line models [34], [35], and equivalent multi-shell models [36]. Incorporating the quantum mechanical behavior of CNT's with a transmission line model leads to a hybrid approach [37]. Further, full-wave, finite element models can include both the quantum mechanical properties of CNTs as well as mutual interactions between CNTs in the bundle [29], [38], [39], [40].

5.3.6 Iterative optimization approach

Biologically-inspired, iterative optimization approaches such as genetic algorithms and neural networks provide another strategy for extraction of circuit parameters from device measurements [41]. Such approaches do not replace, but rather complement the development of and validation of models that has been described above. Iterative optimization approaches have been widely used before to design RF circuits [42], [43], calculate two-port error boxes in calibrated measurements [44] and generate models of nonlinear, large-signal devices [45]. They are especially well suited for generation of simple RF circuits from calibrated broadband measurements because it is not likely that the inverse problem is going to have a unique global solution. There is a multitude of different possible circuits consistent with the measured data. Iterative optimization approaches provide an automated way to explore this wide space of possible circuit models without invoking full wave simulations.

We illustrate a basic example of an iterative approach with a genetic algorithm that generates a lumped element model of a GaN nanowire device from calibrated scattering parameter measurements [41]. Though the nanowire device is used as an example here, iterative optimization approaches may be extended to materials characterization, such as frequency-dependent determination of parameters like complex permittivity and permeability of ferroelectric, ferromagnetic or multiferroic materials, especially in thin film forms [46]. These methods may also be extended to interconnects, such as CNT bundle devices discussed above [47], as well as active devices. In the basic example discussed here, the circuit parameters are represented by a small number of cascaded elements, each representing a circuit element. For a given circuit model, the scattering parameters are calculated by generating an ABCD matrix for each element, cascading all of the elements, and transforming the resulting matrix to a scattering parameter representation. Initially, the algorithm randomly generates a population of candidate circuit models from a pool of available elements. For the GaN nanowire devices, this pool included lumped elements such as series resistors, shunt capacitors, and transmission line elements, with possible ranges of parameter values defined based on reasonable values found in the literature [16], [48], [49].

For each generated model within the population, the scattering parameters are simulated and compared with the calibrated device measurements. The genetic approach culls the circuits from the population with the best agreement with the experiment by minimizing a cost function such as

$$c_f = \sum_{m,n} \sum_N ((\Delta_r(f_N))^2 + (\Delta_i(f_N))^2) , \quad (5.13)$$

where

$$\Delta_r(f_N) = \Re(S_{m,n}^{meas}(f_N)) - \Re(S_{m,n}^{sim}(f_N)) \quad (5.14)$$

and

$$\Delta_i(f_N) = \Im(S_{m,n}^{meas}(f_N)) - \Im(S_{m,n}^{sim}(f_N)) . \quad (5.15)$$

In Equations (5.13) through (5.15), m and n are scattering parameter indices ($m=1,2$; $n=1,2$) and f_N represents the N frequencies the measurements were taken. S_{meas} and S_{sim} are the measured and simulated scattering parameters, respectively. The algorithm generates new circuit models by “mating”

and “mutating” the circuit models with the lowest cost function c_f . This process is repeated over many cycles till the results from the generated circuit model are in a good agreement with the calibrated measurements. The process is terminated when the average cost function c_f is equal to or less than a target cost set by the user.

The simple algorithm was used to generate a model for a two-port, GaN nanowire similar to the Pt nanowire device discussed earlier. The comparison of the measured S parameters with the simulated parameters from the circuit model is shown in Fig. 5.9. A schematic circuit model obtained for the GaN nanowire is shown in the inset of Fig. 5.9(b). The model lends itself to a simple and reasonable physical interpretation. The central 24.9 k Ω resistor may be interpreted as the intrinsic resistance of the nanowire while the combination of 1.3 k Ω resistances in parallel with the capacitances may be interpreted as contact impedances to the nanowire. That said, one should be wary of over-interpretation of the results. Though this circuit model is empirically found to be consistent with the measurements, but it does not guarantee that the chosen model is globally optimal or the “best” circuit model that could be used. Still, an approach such as this provides some insight into overall device behavior. Further, it may be useful to have a model that is consistent with the measurements, independent of the physical interpretation.

References

- [1] G. W. Hanson, "Fundamental transmitting properties of carbon nanotube antennas," *IEEE Transactions on Antennas and Propagation* **53** (2005) pp. 3426-3435.
- [2] C. Rutherglen and P. J. Burke, "Nanoelctromagnetics: Circuits and electromagnetic properties of carbon nanotubes," *Small* **8** (2009) pp. 884-906.
- [3] U. Yogeswaran and S. Chen, "A Review on the Electrochemical Sensors and Biosensors Composed of Nanowires as Sensing Material," *Sensors* **8** (2008) pp. 290-313.
- [4] S. Fiedler, M. Zwanzig, R. Schnidt and W. Scheel, "Nanowires in electronics packaging," in *Nanopackaging: Nanotechnologies and Electronics Packaging*, J. E. Morris, Ed. (Springer US, 2009).
- [5] A. R. Rathmell, S. M. Bergin, Y. - . Hua, Z. Li and B. J. Wiley, "The Growth Mechanism of Copper Nanowires and Their Properties in Flexible, Transparent Conducting Films," *Advanced Materials* **22** (2010) pp. 3558-3563.
- [6] S. Koo, M. D. Edelstein, Q. Li, C. A. Richter and E. M. Vogel, "Silicon nanowires as enhancement-mode Schottky barrier field-effect transistors," *Nanotechnology* **16** (2005) pp. 1482-1485.
- [7] R. R. Llinas, K. D. Walton, M. Nakao, I. Hunter and P. A. Anquetil, "Neuro-vascular central nervous recording/stimulating system: Using nanotechnology probes," *Journal of Nanoparticle Research* **7** (2005) pp. 111-127.
- [8] A. I. Hochbaum, R. Chen, R. D. Delgado, W. Liang, E. C. Garnett, M. Najarian, A. Majumdar and P. Yang, "Enhanced thermoelectric performance of rough silicon nanowires," *Nature* **451** (2008) pp. 163-167.
- [9] J. J. Boland, "Flexible electronics: Within touch of artificial skin," *Nature Materials* **9** (2010) pp.790-792.
- [10] P. J. Burke, "An RF Circuit Model for Carbon Nanotubes," *IEEE Transactions on Nanotechnology* **2** (2003) pp. 55-58.
- [11] P. J. Burke, "Lüttinger liquid theory as a model of the Gigahertz electrical properties of carbon nanotubes," *IEEE Transactions on Nanotechnology* **1** (2002) pp. 129-144.
- [12] ANSYS HFSS: 3D full-wave electromagnetic field simulation. <http://www.ansoft.com/>
- [13] Burger S. *et al*, "JCMsuite: An adaptive FEM solver for precise simulations in nano-optics," *Integrated Photonics and Nanophotonics Research and Applications* (2008) paper ITuE4.
- [14] ANSYS. Ansoft designer. <http://www.ansoft.com/>
- [15] AWR microwave office: RF/microwave design software. <http://web.awrcorp.com/>

- [16] K. Kim, T. M. Wallis, P. Rice, C.-J. Chiang, A. Imtiaz, P. Kabos, and D. S. Filipovic, "A framework for broadband characterization of individual nanowires," *IEEE Microwave and Wireless Component Letters* **20** (2010) pp. 178 – 180.
- [17] K. Kim, P. Rice, T. M. Wallis, D. Gu, S. Lim, A. Imtiaz, P. Kabos, and D. S. Filipovic, "High-frequency Characterization of Contact Resistance and Conductivity of Platinum Nanowires," *IEEE Transactions on Microwave Theory and Techniques* **59** (2011) pp. 2647-2654.
- [18] Kichul Kim, *Characterization of Carbon Nanotubes and Nanowires and Their Application*, PhD Thesis, University of Colorado, Boulder (2010).
- [19] P. A. Smith, C. D. Nordquist, T. N. Jackson, T. S. Mayer, B. R. Martin, J. Mbindyo, and T. E. Mallouk, "Electric-field assisted assembly and alignment of metallic nanowires," *Applied Physics Letters* **77** (2000) pp. 1399-1401.
- [20] M. E. Toimil Molaes, E. M. Hohberger, C. Scheaflein, R. H. Blick, R. Neumann, and C. Trautmann, "Electrical characterization of electrochemically grown single copper nanowires," *Applied Physics Letters* **82** (2003) pp. 2139-2141.
- [21] J.-F. Lin, J. P. Bird, L. Rotkina, and P. A. Bennet, "Classical and quantum transport in focused-ion-beam-deposited Pt nanointerconnects," *Applied Physics Letters* **82** (2003) pp. 805-804.
- [22] G. De Marzil, D. Iacopino, A. J. Quinn, and G. Redmont, "Probing intrinsic transport properties of single metal nanowires: direct-write contact formation using a focused ion beam," *Journal of Applied Physics* **96** (2004) pp. 3458-3462.
- [23] L. Penate-Quesada, J. Mitra, and P. Dawson, "Non-linear electronic transport in Pt nanowires deposited by focused ion beam," *Nanotechnology* **18** (2007) pp. 215203.
- [24] T. Schwamb, B. R. Burg, N. C. Schirmer, and D. Poulidakos, "On the effect of the electrical contact resistance in nanodevices," *Applied Physics Letters* **92** (2008) art. no. 243106.
- [25] A. F. Mayadas and M. Shatzkes, "Electrical-Resistivity Model for Polycrystalline Films: the Case of Arbitrary Reflection at External Surfaces," *Physical Review B* **1** (1970) pp. 1382-1389.
- [26] J. Hao and G. W. Hanson, "Infrared and Optical Properties of Carbon Nanotube Dipole Antennas," *IEEE Transactions on Nanotechnology* **5** (2006) pp. 766-775.
- [27] P. Rice, T. M. Wallis, S. E. Russek and P. Kabos, "Broadband Electrical Characterization of Multiwalled Carbon Nanotubes and Contacts," *Nano Letters* **7** (2007) pp. 1086-1090.
- [28] S. Saluhuddin, M. Ludstrom, and S. Datta, "Transport effects on signal propagation in quantum wires" *IEEE Transactions on Electron Devices* **52** (2005) pp. 1734-1752.
- [29] N. Srivastava and K. Banerjee, "Performance analysis of carbon nanotube interconnects for VLSI applications," *Proceedings of the IEEE/ACM International Conference on Computer-Aided Design* (2005) pp. 383-390.

- [30] Y. Awano, "Carbon nanotube technologies for LSI via interconnects," *IEICE Trans. Electron.* **E89-C** (2006) pp. 1499-1503.
- [31] M. Nihei, A. Kawabata, D. Kondo, M. Horibe, S. Sato and Y. Awano, "Electrical properties of carbon nanotube bundles for future via interconnects," *Japanese Journal of Applied Physics* **44** (2005) pp. 1626-1628.
- [32] A. Thess, R. Lee, P. Nikolaev, H. Dai, P. Petit, J. Robert, C. Xu, Y. H. Lee, S. G. Kim, A. G. Rinzler, D. T. Colbert, G. E. Scuseria, D. Tomanek, J. E. Fischer and R. E. Smalley, "Crystalline Ropes of Metallic Carbon Nanotubes," *Science* **273** (1996) pp. 483-487.
- [33] M. S. Dresselhaus, G. Dresselhaus and P. Avouris, *Carbon Nanotubes: Synthesis, Structure, Properties, and Applications* (Springer, 2001).
- [34] M. S. Sarto and A. Tamburrano, "Electromagnetic analysis of radiofrequency signal propagation along SWCN bundles," *Proceedings of the Sixth IEEE Conference on in Nanotechnology (IEEE-NANO 2006)* (2006) pp. 201-204.
- [35] M. S. Sarto and A. Tamburrano, "Multiconductor transmission line modeling of SWCNT bundles in common-mode excitation," *Proceedings of 2006 IEEE International Symposium on in Electromagnetic Compatibility (EMC 2006)* (2006) pp. 466-471.
- [36] M. V. Shuba, S. A. Maksimenko and A. Lakhtakia, "Electromagnetic wave propagation in an almost circular bundle of closely packed metallic carbon nanotubes," *Physical Review B* **76** (2007) art. no. 155407.
- [37] M. S. Sarto, A. Tamburrano and M. D'Amore, "New Electron-Waveguide-Based Modeling for Carbon Nanotube Interconnects," *IEEE Transactions on Nanotechnology* **8** (2009) pp. 214-225.
- [38] A. Naeemi, R. Sarvari and J. D. Meindl, "Performance comparison between carbon nanotube and copper interconnects for GSI," *IEDM Technical Digest in Electron Devices Meeting* (2004) pp. 699-702.
- [39] A. Nieuwoudt and Y. Massoud, "Evaluating the impact of resistance in carbon nanotube bundles for VLSI interconnect using diameterdependent modeling techniques," *IEEE Transactions on Electron Devices* **53** (2006) pp. 2460-2466.
- [40] C. W. Tan and Jianmin Miao, "Modeling of carbon nanotube vertical interconnects as transmission lines," *Proceedings of the 2006 IEEE Conference on in Emerging Technologies – Nanoelectronics* (2006) pp. 75-78.
- [41] T. M. Wallis, "A genetic algorithm for generating RF circuit models from calibrated broadband measurements," *Proceedings of the 78th ARFTG Microwave Measurement Symposium 78th ARFTG* (2011) pp.1-5.
- [42] J. G. Pascual, P. F. Quesada, D. C. Rebenaque, J. L. G. Tornero, and A. A. Melcon, "A multilayered shielded microwave circuit design method based on genetic algorithms and neural networks," *2006 IEEE MTT-S International Microwave Symposium Digest* (2006) pp. 1427-1430.

- [43] S. Iezekiel, "Application of evolutionary computation techniques to nonlinear microwave circuit analysis," *Proceedings of the 8th IEEE International Symposium on High Performance Electron Devices for Microwave and Optoelectronic Applications* (2000) pp. 230-235.
- [44] A. S. Adalev, N. V. Korovkin, M. Hayakawa, and J. B. Nitsch, "Deembedding and unterminating microwave fixtures with the genetic algorithm," *IEEE Transactions on Microwave Theory and Techniques* **54** (2006) pp. 3131-3140.
- [45] J. Jargon, K. C. Gupta, D. Schreurs, K. Remley, D. DeGroot, "A method of developing frequency-domain models for nonlinear circuits based on large-signal measurements," *Proceedings of the 58th ARFTG Microwave Measurement Symposium* (2001) pp. 35-48.
- [46] N. Orloff, J. Mateu, M. Murakami, I. Takeuchi, and J. C. Booth, "Broadband characterization of multilayer dielectric thin-films," *2007 IEEE MTT-S International Microwave Symposium Digest (MTT)* (2007) pp. 1177-1180.
- [47] J. J. Plombon, K. P. O'Brien, F. Gstrein, V. M. Dubin, and Y. Jiao, "High-frequency electrical properties of individual and bundled carbon nanotubes," *Applied Physics Letters* **90** (2007) art. no. 063106.
- [48] D. Gu, T. M. Wallis, P. Blanchard, S.-H. Lim, A. Imtiaz, K. A. Bertness, N. A. Sanford, and P. Kabos, "Deembedding parasitic elements of GaN nanowire metal semiconductor field effect transistors by use of microwave measurements," *Applied Physics Letters* **98** (2011) art. no. 223109.
- [49] K. Kim, T. M. Wallis, P. Rice, C.-J. Chiang, A. Imtiaz, P. Kabos, and D. Filipovic, "Modeling and metrology of metallic nanowires with application to microwave interconnects," *2010 IEEE MTT-S International Microwave Symposium Digest (MTT)* (2010) pp. 1292-1295.

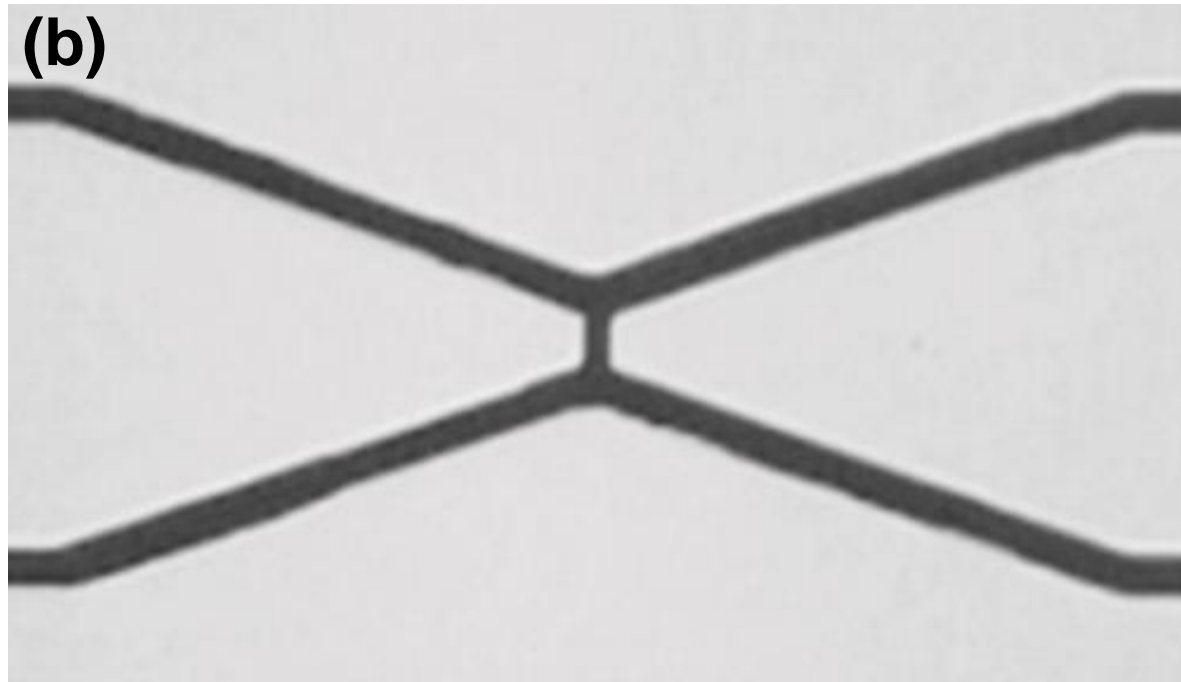
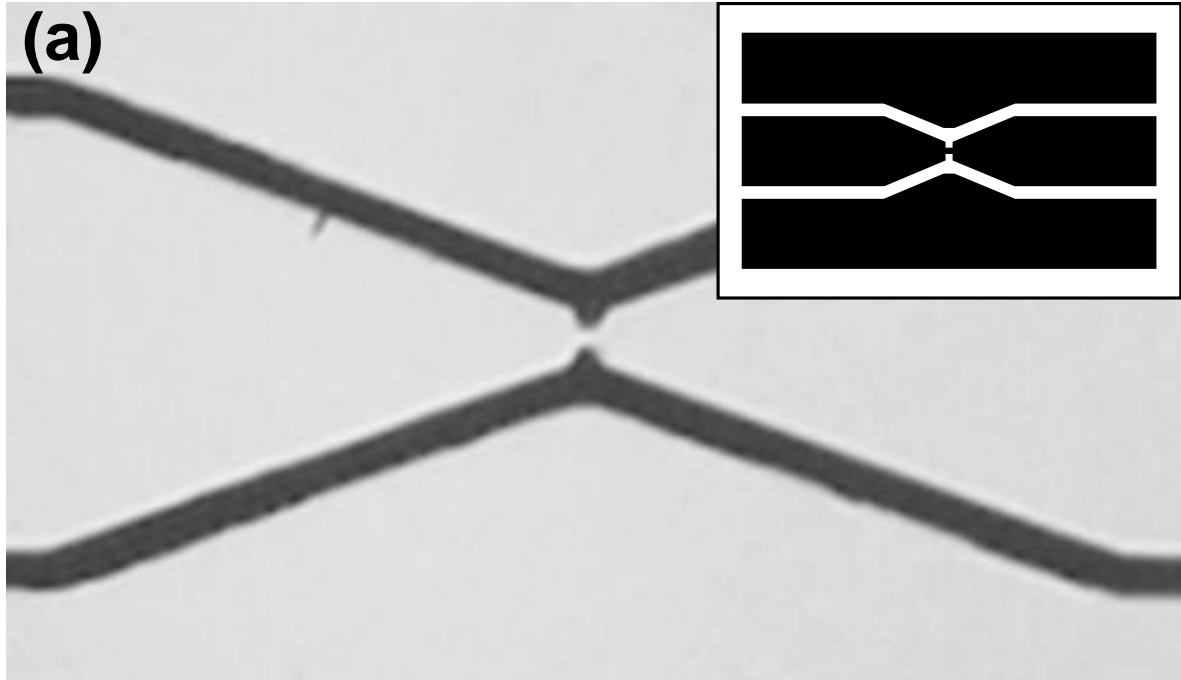
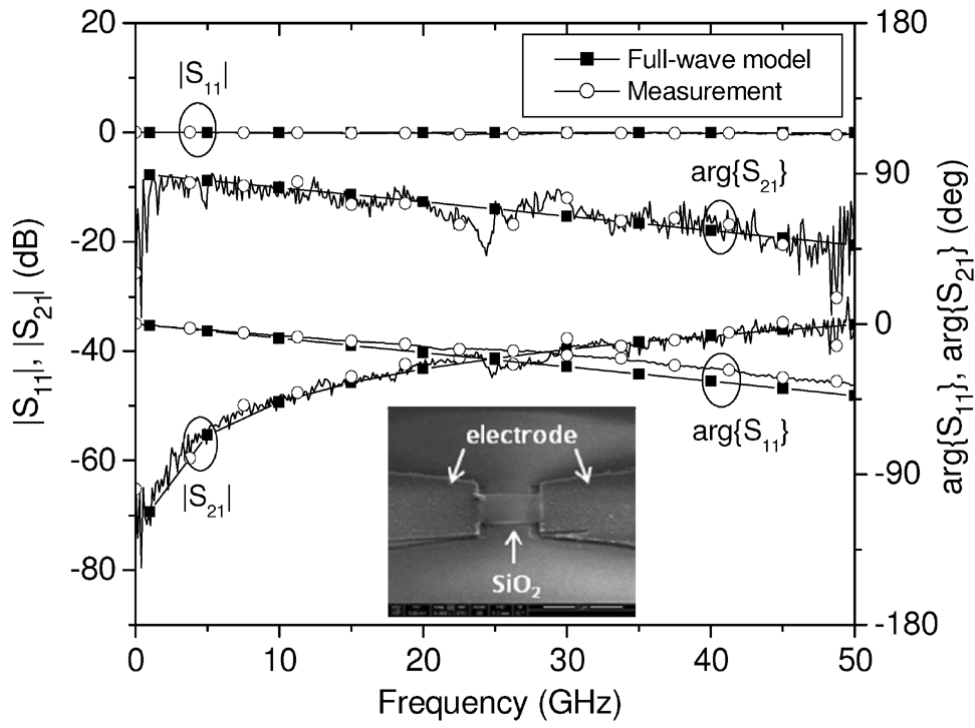
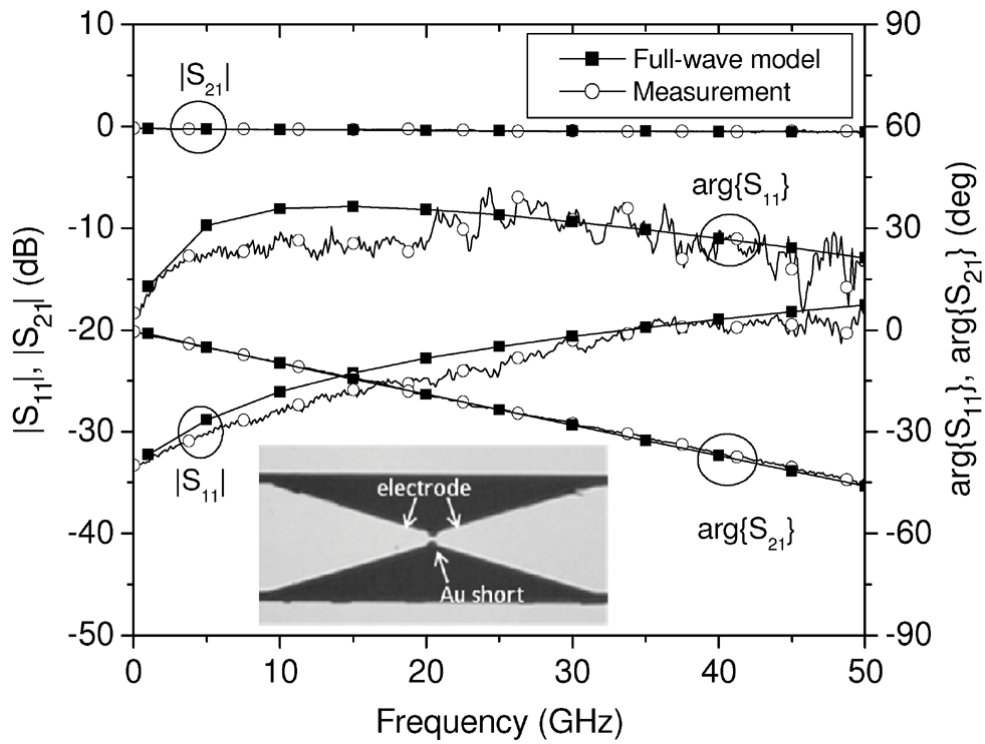


FIGURE 5-1.



(a)



(b)

Figure 52

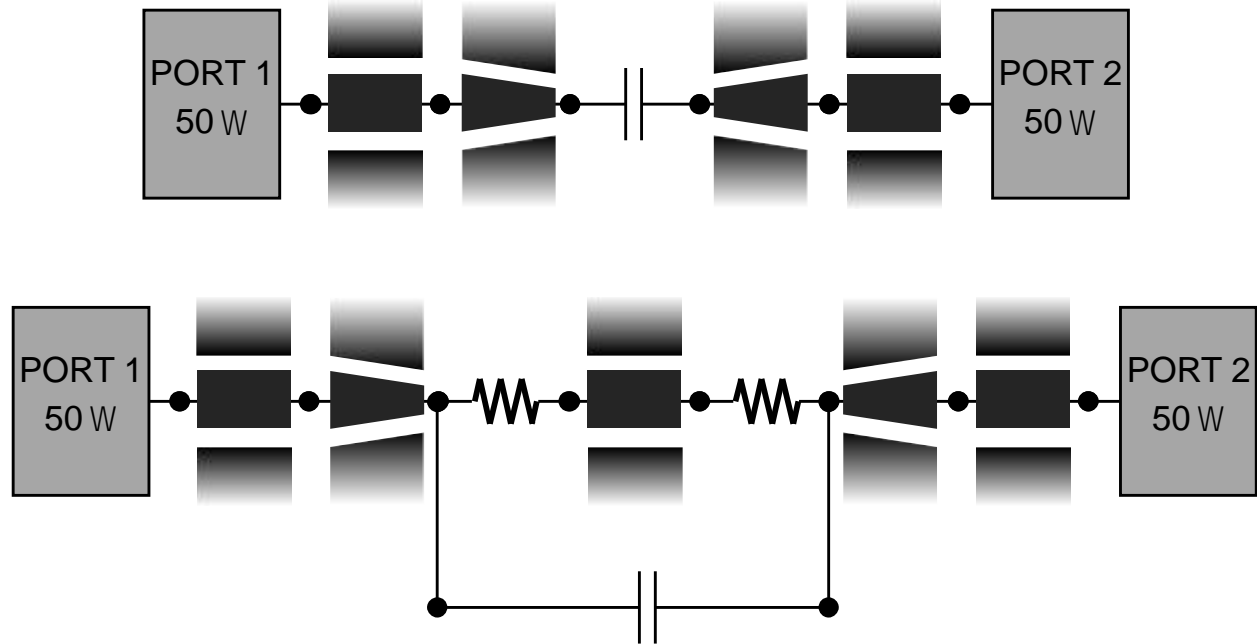


FIGURE 5.3

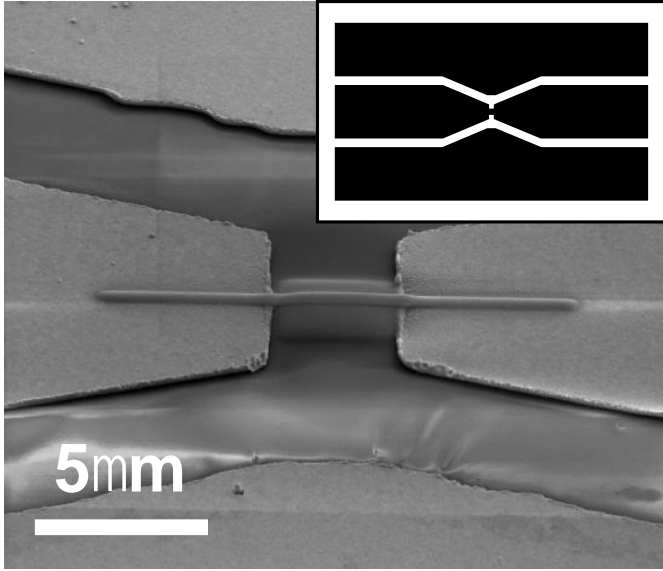


FIGURE 5-4.

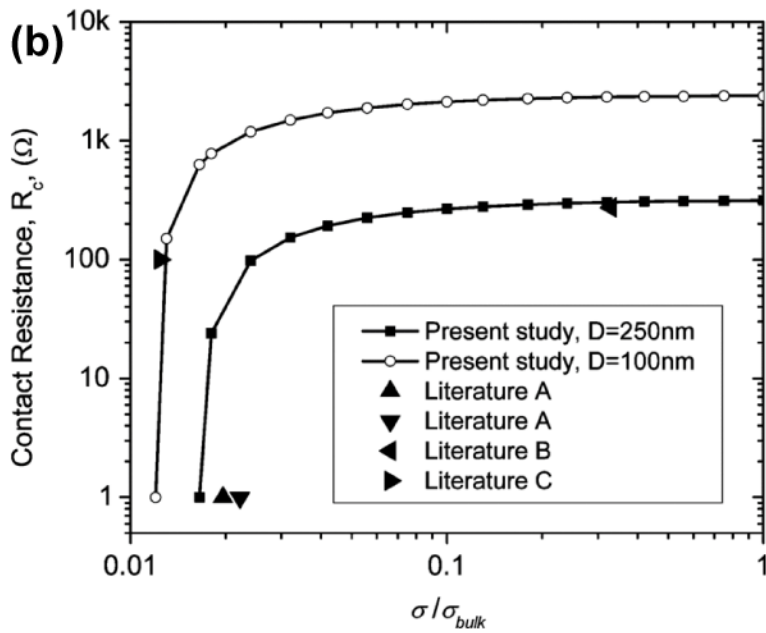
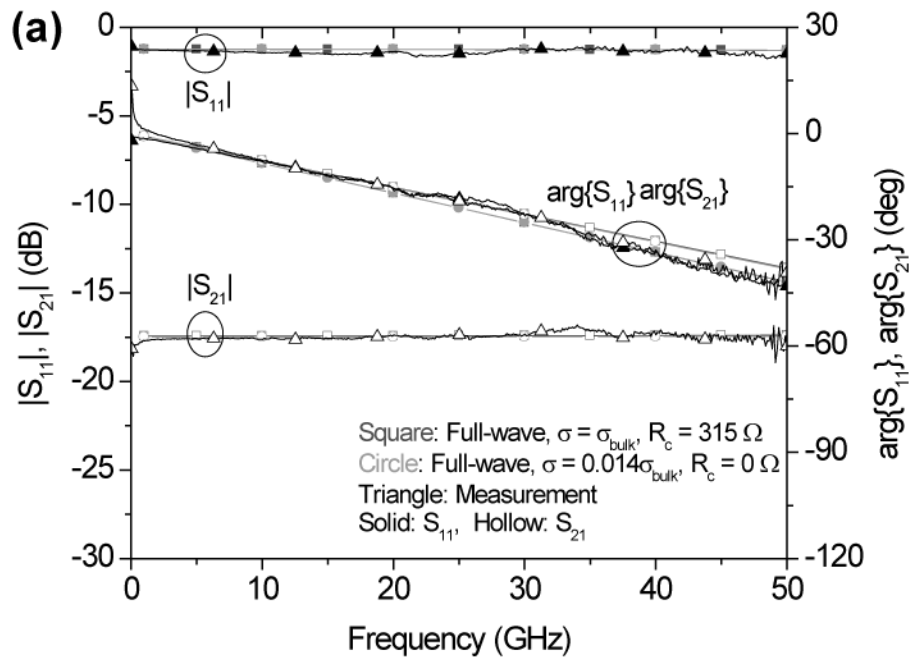


Figure 5.5

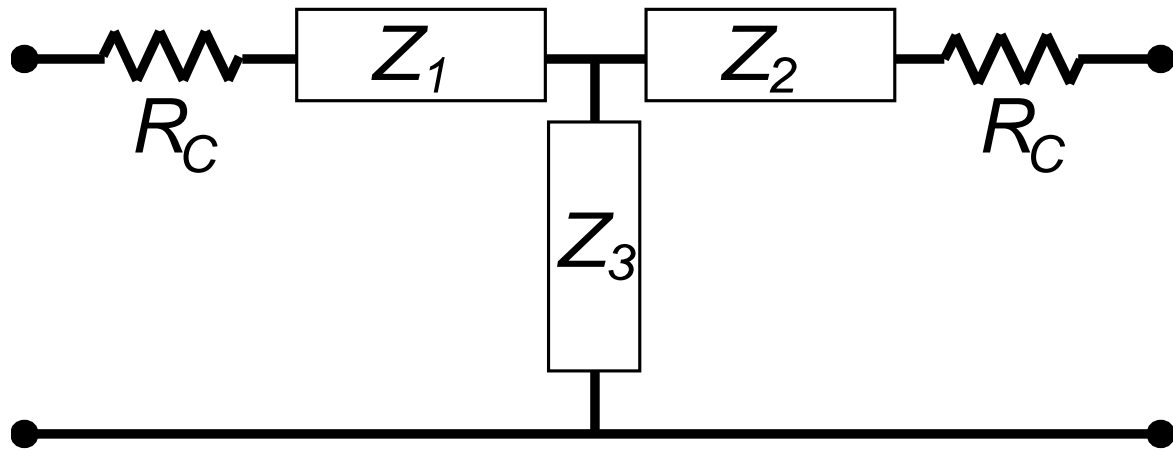


FIGURE 5.6

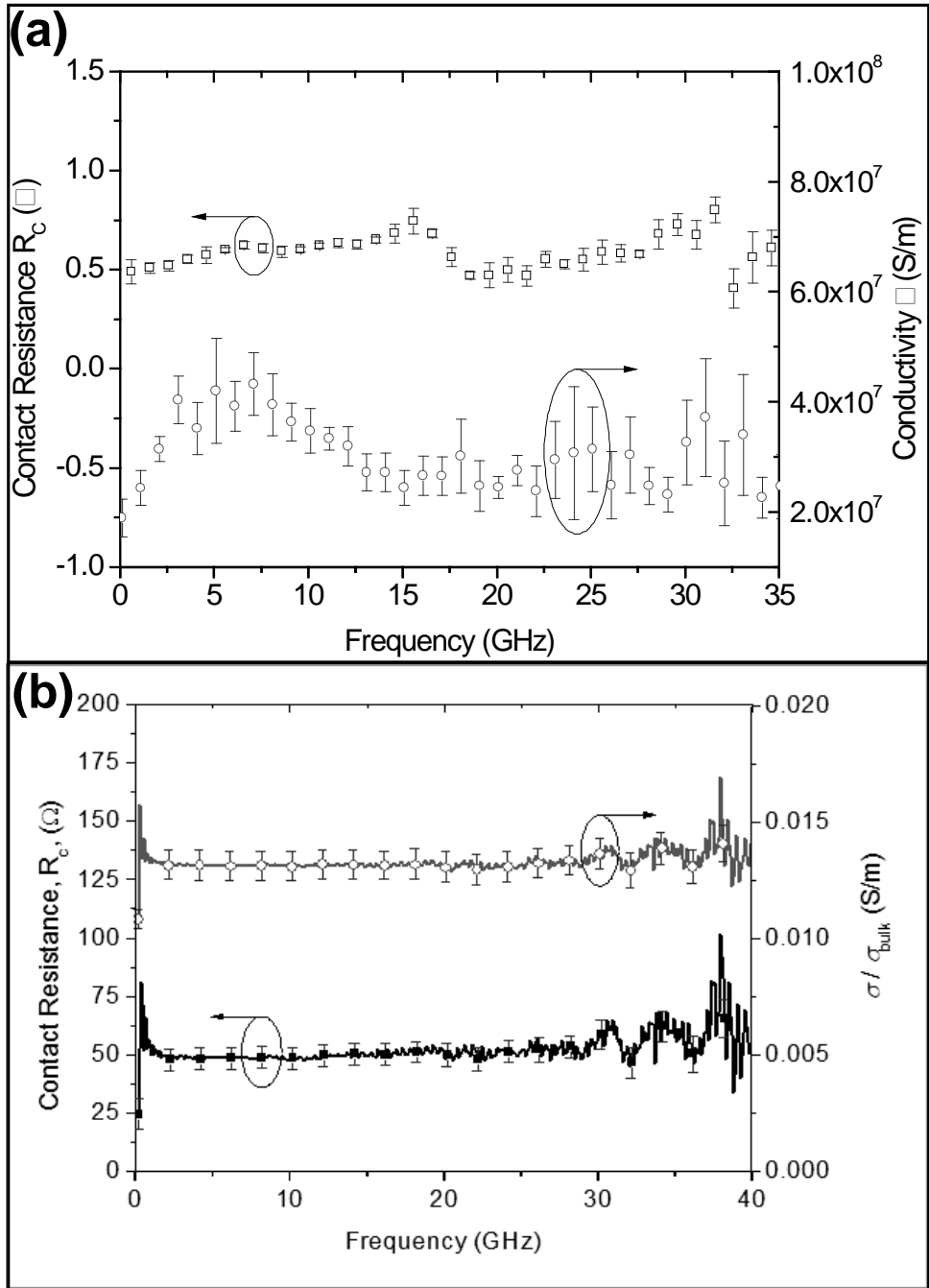


Figure 57

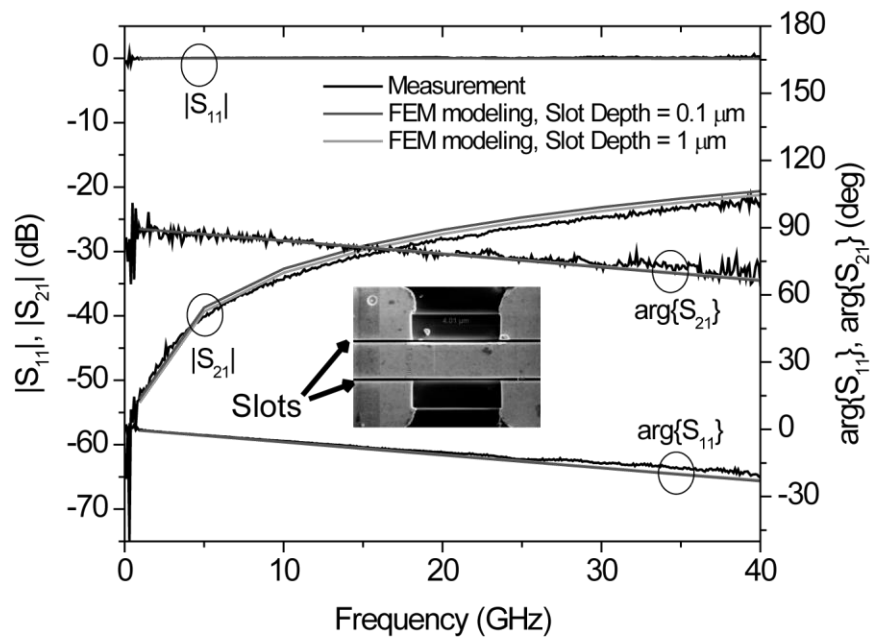


Figure 5.8

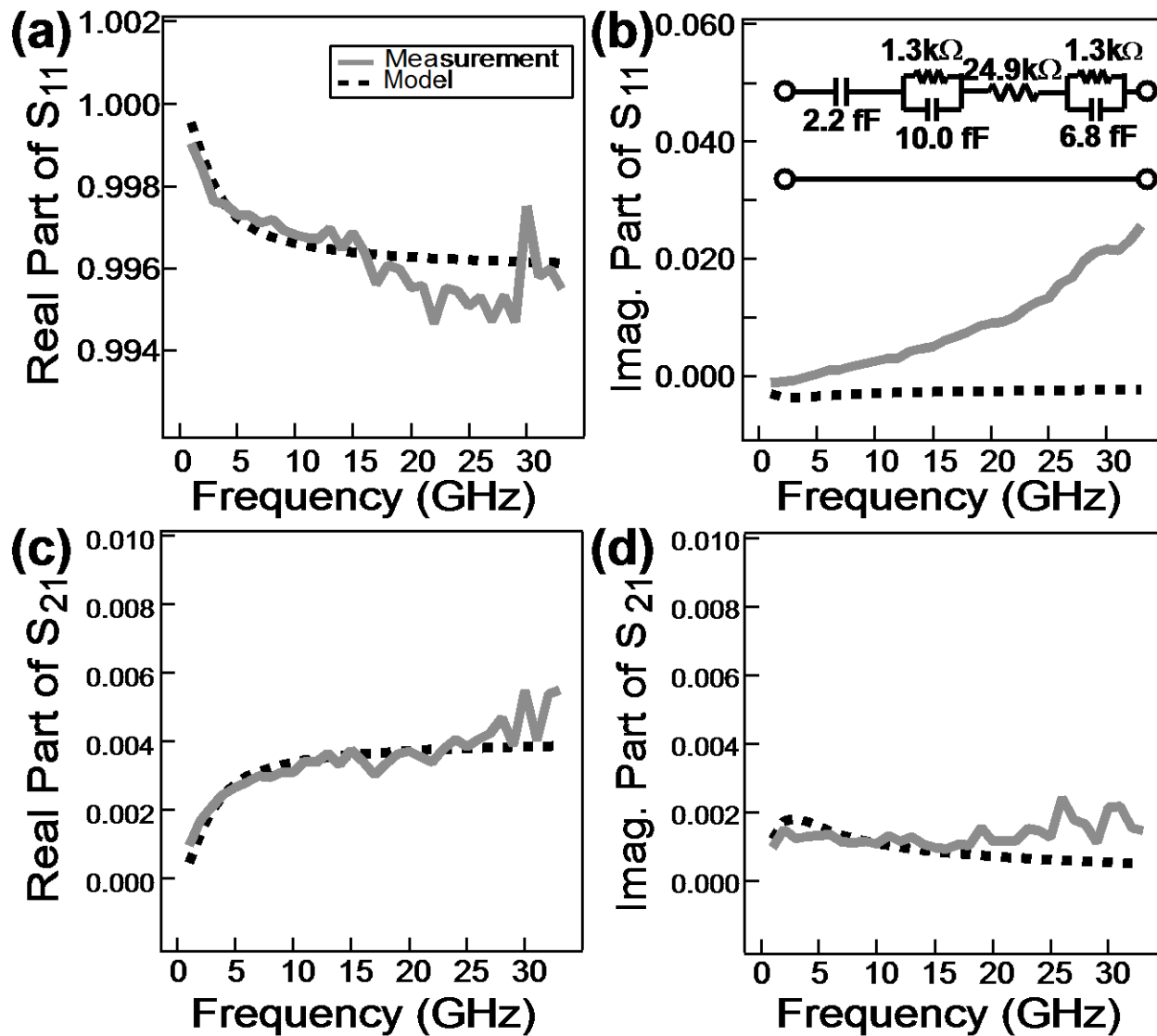


FIGURE 5.9